

High-Frequency Space Diffusion Model for Accelerated MRI

Chentao Cao, Zhuo-Xu Cui, Shaonan Liu, Hairong Zheng, *Senior Member, IEEE*,
Dong Liang, *Senior Member, IEEE*, Yanjie Zhu, *Member, IEEE*

Abstract—Diffusion models with continuous stochastic differential equations (SDEs) have shown superior performances in image generation. It can be used as a deep generative prior to solve the inverse problem in MR reconstruction. However, the existing VP-SDE can be treated as maximizing the energy of the MR image to be reconstructed and may lead to SDE sequence divergence. The VE-SDE based MR reconstruction is not consistent with actual diffusion process. In addition, both VE- and VP-SDEs-based models suffer from a time-consuming sampling procedure, resulting long reconstruction time. In this study, a new SDE focusing on the diffusion process in high-frequency space is designed specifically for robust MR reconstruction based on diffusion models. Experiments on the publicly fastMRI dataset show that HFS-SDE based reconstruction method outperforms the parallel imaging, supervised deep learning, and existing VE- and VP-SDEs-based methods in terms of reconstruction accuracy. It also improves the stability of MR reconstruction and accelerates sampling procedure of reverse diffusion.

Index Terms—Diffusion Models, MRI, Image Reconstruction, Inverse Problem

I. INTRODUCTION

MAGNETIC resonance imaging (MRI) is a powerful tool of medical imaging but suffers from a long acquisition time. The main strategy for accelerating MR scan is to undersample the k-space data and then reconstruct images based on priors of images and measurements, as in parallel imaging and compressed sensing (CS) [1]–[9].

In recent years, deep learning (DL)-based reconstruction methods have grown in popularity and shown great potential to remove aliasing artifacts caused by undersampling [10]–[17]. One board family of DL-based methods is supervised learning technique. This technique takes measured k-space data and

images to be reconstructed as the inputs and outputs of a deep neural network, and directly learns the mapping between them. Typical network architectures are based on unrolling that unroll an iterative solution of CS optimization into a network by learning the hyper-parameters and regularizations, e.g. ISTA-Net, ADMM-Net [18]–[21]. Supervised learning techniques are usually trained for a specific imaging model or anatomy, and show excellent performance in these tasks. However, generalization is one of the major bottlenecks of supervised learning methods. The trained network may show severely degraded reconstruction quality when applied out of distribution.

Another approach of DL-based reconstruction methods is unsupervised learning technique based on distribution learning. It uses the data distribution predicted by a deep generative model as priors to solve the inverse problem of MR reconstruction. This technique adapts to changes in measurements easily because they are trained without references to measurements. Recently, diffusion models have shown significant progress and have become the new state-of-the-art (SOTA) deep generative models [22]–[25]. Two successful classes of diffusion models, i.e. denoising diffusion probabilistic models (DDPMs) [26] and score matching with Langevin dynamic (SMLD) [27], have gained wide interest and demonstrated remarkable synthesis quality. Song [28] encapsulated these two approaches into a generalized framework of score-based generative models based on continuous stochastic differential equations (SDEs), improving the capabilities of diffusion models. SMLD and DDPM correspond to Variance Exploding (VE) SDE and Variance Preserving (VP) SDE, respectively. Under the framework of score-based SDEs, data distribution is transformed to a tractable distribution (i.e. Gaussian noise distribution) by a forward SDE. This process can be reversed for sample generation based on a reverse-time SDE derived from the forward SDE, given the score function of the marginal probability densities. Score-based SDEs have been adopted to inverse problem of MR reconstruction and have shown impressive results [29]–[34].

However, there exist some pitfalls of diffusion model-based MR reconstructions that received little attention in prior works. The origin VE- and VP-SDEs were not proposed specifically for MR reconstruction. When using VE-SDE, the mean of the perturbed data is kept constant during the forward process, deriving that the means of $\mathbf{x}(0)$ and $\mathbf{x}(T)$ are the same. Vice versa, the mean of $\mathbf{x}(0)$ should also be equal to the mean of the initial value $\mathbf{x}(T)$ in the reverse process of VE-SDE. However,

Chentao Cao and Zhuo-Xu Cui contributed equally to this manuscript.
Corresponding author: yj.zhu@siat.ac.cn (Yanjie Zhu).

Chentao Cao, Hairong Zheng, Dong Liang and Yanjie Zhu are with Lauterbur Research Center for Biomedical Imaging, Shenzhen Institutes of Advanced Technology, Chinese Academy of Sciences, Shenzhen, China (e-mail: ct.cao@siat.ac.cn; yj.zhu@siat.ac.cn).

Chentao Cao is also with University of Chinese Academy of Sciences, Beijing, China.

Yanjie Zhu is also with National Center for Applied Mathematics Shenzhen (NCAMS), Shenzhen, China.

Zhuo-Xu Cui and Dong Liang are with Research Center for Medical AI, Shenzhen Institutes of Advanced Technology, Chinese Academy of Sciences, Shenzhen, China (e-mail: zx.cui@siat.ac.cn; dong.liang@siat.ac.cn).

Dong Liang is also with Pazhou Lab, Guangzhou, China.

Shaonan Liu is with Inner Mongolia University, Inner Mongolia, China.

VE-SDE-based MR reconstruction typically starts from zero-mean Gaussian noise in the reverse diffusion process, which is inconsistent with the forward process and may generate fake structures of reconstructed images. In contrast, the forward diffusion process of VP-SDE-based MR reconstruction gradually decays $\mathbf{x}(0)$ while adding Gaussian noise, and the mean of $\mathbf{x}(T)$ converges to 0 eventually. This process is consistent with the actual diffusion process. Therefore, VP-SDE may avoid the above issue in VE-SDE and more suitable for MR reconstruction than VE-SDE in terms of the confidence. However, the reverse process of VP-SDE can be treated as maximizing the energy of the MR image to be reconstructed, which may lead to SDE sequence divergence and be unstable for MR reconstruction (details in Section II-C).

Additionally, both VE- and VP-SDEs-based models suffer from a long sampling procedure, requiring thousands of iterations to produce high-quality samples. The choice of the initial value of the optimization iteration algorithm has a significant impact on the convergence speed, but unfortunately, the initial value of reverse-time VE- and VP-SDEs does not utilize the undersampled data in fast MR reconstruction.

In this study, a new SDE focusing on the diffusion process in high-frequency space (HFS-SDE), is designed specifically for fast and robust MR reconstruction. Specifically, its reverse process starts from high-frequency noise accompany with acquired low-frequency k-space data, resulting in fewer sampling steps than existing VP- and VE-SDEs starting from Gaussian noise. At the same time, this reverse process can be treated as only maximizing the high-frequency energy of the MR image, thus largely reduce the divergence risk and improve the stability of MR reconstruction. Experiments show that MR reconstruction using HFS-SDE can achieve better performance.

A. Contributions

- 1) We propose a new SDE (HFS-SDE) for diffusion model-based MR reconstruction with high stability. When applied to multi-coil MR data, we achieve a 12-fold uniform acceleration in 2D imaging.
- 2) We show that high-quality reconstructions can be obtained using HFS-SDE with only 100 sampling steps, meaning the sampling procedure is highly accelerated.
- 3) The experiments show that more image details are preserved using HFS-SDE than using VE- and VP-SDEs, since the diffusion process focuses on high-frequency.

The following sections of the paper are organized as follows: Section II introduces background, Section III describes the proposed method and Section IV provides the experimental results. Discussion and conclusion are given in Section V and Section VI.

II. BACKGROUND

A. Problem Formulation

The imaging model of MR reconstruction can be formulated as:

$$\mathbf{y} = \mathbf{A}\mathbf{x} + \epsilon \quad (1)$$

where \mathbf{y} is the undersampled measurements in the frequency domain (k-space), \mathbf{x} is the image to be reconstructed, \mathbf{A} denotes the encoding matrix, $\mathbf{A} = \mathbf{M}\mathbf{F}\mathbf{S}$, \mathbf{M} is the under-sampling operator, \mathbf{F} denotes the Fourier operator, \mathbf{S} denotes the coil sensitivity, and $\epsilon \sim \mathcal{N}(0, \sigma_\epsilon^2)$. For 2D image, $\mathbf{x} \in \mathbb{R}^n$, $\mathbf{y} \in \mathbb{R}^m$ and $\mathbf{A} \in \mathbb{R}^{m \times n}$.

Eq. (1) can be formulated as an optimization problem:

$$\mathbf{x}^* = \arg \min_{\mathbf{x}} \frac{1}{2} \|\mathbf{A}\mathbf{x} - \mathbf{y}\|_2^2 + \mathcal{R}(\mathbf{x}) \quad (2)$$

$\mathcal{R}(\mathbf{x})$ is the prior constraint of the MR image.

B. Score-based SDE

In score-based SDE [28], the diffusion process $\{\mathbf{x}(t)\}_{t=0}^T$ is continuous with a time variable $t \in [0, T]$, and thus can be constructed as the solution of a SDE. The corresponding reverse process can be accurately modeled with a reverse-time SDE of the forward one, extending the capability of diffusion models. The reverse-time SDE can be approximated by training a network to estimate the score of the densities at each time step, and then used for sample generation using numerical SDE solvers.

The diffusion process can be described as the solution of the following SDE:

$$d\mathbf{x} = \mathbf{f}(\mathbf{x}, t)dt + g(t)d\mathbf{w} \quad (3)$$

where \mathbf{f} and g are the drift and diffusion coefficients of \mathbf{x} , respectively. \mathbf{w} is the standard Wiener process. The reverse process is also a diffusion process, modeled by the following reverse-time SDE:

$$d\mathbf{x} = [\mathbf{f}(\mathbf{x}, t) - g(t)^2 \nabla_{\mathbf{x}} \log p_t(\mathbf{x})] dt + g(t)d\bar{\mathbf{w}} \quad (4)$$

where $\nabla_{\mathbf{x}} \log p_t(\mathbf{x})$ is known as the score function, $\bar{\mathbf{w}}$ is the standard Wiener process when the time goes back to 0 from T .

In order to solve Eq. (2), the score function $\nabla_{\mathbf{x}} \log p_t(\mathbf{x})$ can be estimated by a neural network $\mathbf{s}_\theta(\mathbf{x}(t), t)$ with the loss function of

$$\theta^* = \arg \min_{\theta} \mathbb{E}_t \left\{ \lambda(t) \mathbb{E}_{\mathbf{x}(0)} \mathbb{E}_{\mathbf{x}(t)|\mathbf{x}(0)} [\|\mathbf{s}_\theta(\mathbf{x}(t), t) - \nabla_{\mathbf{x}(t)} \log p_{0t}(\mathbf{x}(t) | \mathbf{x}(0))\|_2^2] \right\} \quad (5)$$

where $\lambda(t)$ is a positive weighting function, t is uniformly sampled over $[0, T]$, $\mathbf{x}(0) \sim p_{\text{data}}$ and $\mathbf{x}(T) \sim p_{\text{noise}}$. $p_{0t}(\mathbf{x}(t) | \mathbf{x}(0))$ is the perturbation kernel. Once the score model $\mathbf{s}_\theta(\mathbf{x}(t), t)$ is trained by Eq. (5), the image can be generated by the reverse diffusion process.

For VE-SDE and VP-SDE, the SDEs of the forward processes are:

$$\begin{cases} d\mathbf{x} = \sqrt{\frac{d[\sigma^2(t)]}{dt}} d\mathbf{w} & \text{(VE-SDE)} \\ d\mathbf{x} = -\frac{1}{2}\beta(t)\mathbf{x}dt + \sqrt{\beta(t)}d\mathbf{w} & \text{(VP-SDE)} \end{cases} \quad (6)$$

C. Score-based SDEs for MRI Reconstruction

Score-based SDEs have been applied for MR reconstruction [30], [31], [35]–[37]. Specifically, the stochastic samples from the image distribution can be generated via posterior sampling, instead of directly modeling the prior information as in Eq. (2).

Given the undersampled k-space data \mathbf{y} , MR images can be generation through the reverse-time SDE:

$$d\mathbf{x} = \{\mathbf{f}(\mathbf{x}, t) - g(t)^2 \nabla_{\mathbf{x}} \log p_t(\mathbf{x} | \mathbf{y})\} dt + g(t) d\bar{\mathbf{w}} \quad (7)$$

Here, \mathbf{x} is the image to be reconstructed.

During the forward diffusion process, VE-SDE adds Gaussian noise with zero mean and gradually increasing variance to the data $\mathbf{x}(0)$. The perturbation kernel $p_{0t}(\mathbf{x}(t) | \mathbf{x}(0))$ of VE-SDE is:

$$p_{0t}(\mathbf{x}(t) | \mathbf{x}(0)) = \mathcal{N}(\mathbf{x}(t); \mathbf{x}(0), [\sigma^2(t) - \sigma^2(0)]\mathbf{I}) \quad (8)$$

$\mathbf{x}(0)$ is the data distribution and $\mathbf{x}(t)$ denotes the perturbed data at the moment t , $\mathbf{x}(0) \sim p_0(\mathbf{x})$. The perturbation kernel indicates the mean of $\mathbf{x}(t)$ is always the same as $\mathbf{x}(0)$. Full sampled images (i.e. $\mathbf{x}(0)$) are not available in MRI reconstruction. Theoretically, the reverse-time VE-SDE-based MR reconstruction requires $\mathbf{x}(0)$ plus Gaussian noise as the initial value, which is difficult to perform in reality.

When using VP-SDE, the iterative rule of the reverse-time SDE is

$$\mathbf{x}_i = \mathbf{x}_{i+1} + \frac{1}{2}\beta_{i+1}\mathbf{x}_{i+1} + \beta_{i+1}\mathbf{s}_{\theta^*}(\mathbf{x}_{i+1}, i+1) + \sqrt{\beta_{i+1}}\mathbf{z}_i, \quad i = 0, 1, \dots, N-1 \quad (9)$$

where \mathbf{x}_0 is considered to be the reconstructed MR image, $\mathbf{s}_{\theta^*}(\mathbf{x}_{i+1}, i+1)$ is the trained score-based model, $\mathbf{z}_i \sim \mathcal{N}(\mathbf{0}, \mathbf{I})$ and $\{\beta_1, \beta_2, \dots, \beta_N\}$ are given coefficients to control the noise level. From optimization perspective, the reverse-time VP-SDE can be viewed as the Stochastic gradient Langvien descent algorithm for the optimization problem (stochasticity is introduced by Gaussian noise \mathbf{z}):

$$\max_{\mathbf{x}} \lambda_1 e^{\|\mathbf{x}\|^2} + \lambda_2 e^{\log p(\mathbf{x})}, \quad (10)$$

where λ_1 and λ_2 are positive weights, $\nabla_{\mathbf{x}} \log p(\mathbf{x})$ is approximated by score-based model $\mathbf{s}_{\theta^*}(\mathbf{x})$. Since the existence of $\lambda_1 e^{\|\mathbf{x}\|^2}$, and we cannot know the exact expression of the data distribution $p(\mathbf{x})$, there is a possibility of energy explosion of \mathbf{x} (i.e. $\|\mathbf{x}\| \rightarrow \infty$). Since energy of the image is mainly concentrated in the low-frequency space, diffusion process restricted to high-frequency space may reduce the divergence of SDE sequence.

III. THEORY AND METHODS

A. The Proposed Methods: High-Frequency Space Diffusion Model

This section introduces the proposed HFS-SDE first, then describe how to train the score network and reconstruct MR images according to the reverse-time HFS-SDE. Fig. 1 shows the framework of the HFS-SDE based MR reconstruction.

1) *The High-Frequency Space SDE*: To restrict the diffusion process in high-frequency space, we first construct high- and low-frequency operators $\mathcal{F}_h(\cdot)$ and $\mathcal{F}_l(\cdot)$ as follows:

$$\begin{cases} \mathcal{F}_h(\cdot) := \mathbf{F}^{-1}((\mathbf{I} - \mathbf{M}_l) \cdot \mathbf{F}(\cdot)) \\ \mathcal{F}_l(\cdot) := \mathbf{F}^{-1}(\mathbf{M}_l \cdot \mathbf{F}(\cdot)) \end{cases} \quad (11)$$

where \mathbf{M}_l is the mask to differentiate low- and high-frequency spaces, with value 1 for k-space center (suppose the area size is $n_l \times n_l$) and 0 for the rest of the region (high-frequency region). \mathbf{I} denotes all-ones matrix ($(\mathbf{I} - \mathbf{M}_l)$ is shown in Fig. 1 (b)). In an extreme case $n_l = 0$, HFS-SDE is downgraded to VP-SDE and in this study, we choose $n_l = 24$. In the multi-coil scenario,

$$\begin{cases} \mathcal{F}_h(\mathbf{x}) := \sum_{j=1}^n \text{csm}_j^* \cdot \mathbf{F}^{-1}((\mathbf{I} - \mathbf{M}_l) \cdot \mathbf{F}(\text{csm}_j \cdot \mathbf{x}_i)) \\ \mathcal{F}_l(\mathbf{x}) := \sum_{j=1}^n \text{csm}_j^* \cdot \mathbf{F}^{-1}(\mathbf{M}_l \cdot \mathbf{F}(\text{csm}_j \cdot \mathbf{x}_i)) \end{cases} \quad (12)$$

n indicates the number of coils, csm_j denotes the sensitivity of the j th coil and \mathbf{x} denotes the MR image.

Assuming that there are N noise scales in the forward diffusion process constructed by the following discrete Markov chain,

$$\mathbf{x}_i = \mathcal{F}_l(\mathbf{x}_{i-1}) + \sqrt{1 - \beta_i} \mathcal{F}_h(\mathbf{x}_{i-1}) + \sqrt{\beta_i} \mathcal{F}_h(\mathbf{z}_{i-1}), \quad i = 1, \dots, N \quad (13)$$

$\{\beta_1, \beta_2, \dots, \beta_N\}$ are given coefficients to control the noise level and $\mathbf{z}_{i-1} \sim \mathcal{N}(\mathbf{0}, \mathbf{I})$. As $\Delta t = \frac{1}{N} \rightarrow 0$, Eq. (13) converges to the following SDE (detailed in Appendix A):

$$d\mathbf{x} = -\frac{1}{2}\beta(t)\mathcal{F}_h(\mathbf{x})dt + \sqrt{\beta(t)}\mathcal{F}_h d\mathbf{w} \quad (14)$$

By Särkkä, Simo [38] and let $\beta(t) = \bar{\beta}_{\min} + t(\bar{\beta}_{\max} - \bar{\beta}_{\min})$ for $t \in [0, 1]$, the perturbation kernel of HFS-SDE can be derived as

$$\begin{aligned} p_{0t}(\mathbf{x}(t) | \mathbf{x}(0)) &= \mathcal{N}(\mathbf{x}(t); e^{(-\frac{1}{4}t^2(\bar{\beta}_{\max} - \bar{\beta}_{\min}) - \frac{1}{2}t\bar{\beta}_{\min})\mathcal{F}_h} \mathbf{x}(0), \\ &\quad \mathbf{I} - \mathbf{I}e^{(-\frac{1}{2}t^2(\bar{\beta}_{\max} - \bar{\beta}_{\min}) - t\bar{\beta}_{\min})\mathcal{F}_h}), \quad t \in [0, 1] \end{aligned} \quad (15)$$

where the mean μ and covariance matrix Σ are exponential functions with the high-frequency operator \mathcal{F}_h in the exponent.

Specifically, the calculation of the exponential operator requires a spectral decomposition of \mathcal{F}_h . Due to the large dimension of \mathcal{F}_h , the computational complexity of the spectral decomposition is intolerable. Therefore, we proposed an approximate method to calculate it. Let the coefficient before \mathcal{F}_h to be k . The exponential function with \mathcal{F}_h can be expanded using Taylor expansion:

$$e^{k\mathcal{F}_h} = \prod_{i=0}^L e^{\frac{k}{L}\mathcal{F}_h} = \prod_{i=0}^L \left(\mathbf{I} + \frac{k}{L}\mathcal{F}_h + o\left(\frac{1}{L}\right)\mathcal{F}_h^2 \right), \quad (16)$$

This function involves massive calculations and is still difficult to implement. Thanks to $\mathcal{F}_h(\cdot)^2 = \mathcal{F}_h(\cdot)$, we can get

$$\lim_{L \rightarrow \infty} \prod_{i=0}^L \left(\mathbf{I} + \frac{k}{L}\mathcal{F}_h + o\left(\frac{1}{L}\right)\mathcal{F}_h^2 \right) = (e^k - 1)\mathcal{F}_h + \mathbf{I} \quad (17)$$

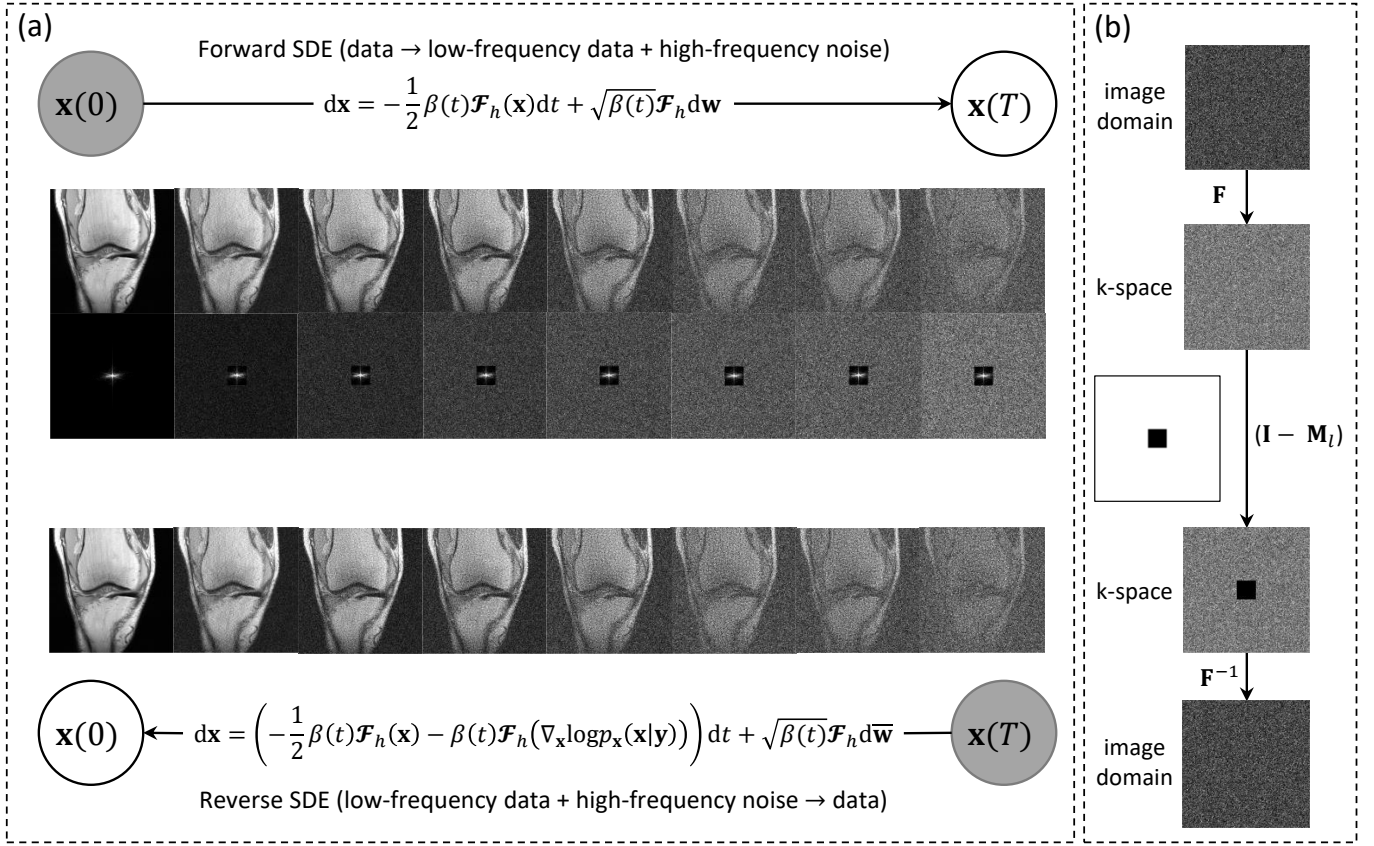


Fig. 1: Illustrate the proposed high-frequency space diffusion model. (a) In the forward process, high-frequency noises with multiple scales are added to the data (first row). The second row shows the k-space corresponding to the perturbed data (no noise is added to the central region of k-space). (b) Demonstrate the steps to acquire high-frequency noise. High-frequency noise is added to the data in the image domain.

Then the mean $\boldsymbol{\mu}$ and covariance matrix $\boldsymbol{\Sigma}$ of the perturbation kernel can be re-expressed as

$$\begin{cases} \boldsymbol{\mu} = \left(e^{(-\frac{1}{4}t^2(\bar{\beta}_{\max}-\bar{\beta}_{\min})-\frac{1}{2}t\bar{\beta}_{\min})} - 1 \right) \mathcal{F}_h(\mathbf{x}(0)) + \mathbf{x}(0) \\ \boldsymbol{\Sigma} = \left(1 - e^{-\frac{1}{2}t^2(\bar{\beta}_{\max}-\bar{\beta}_{\min})-t\bar{\beta}_{\min}} \right) \mathcal{F}_h \end{cases} \quad (18)$$

2) Estimate Score for HFS-SDE: Once the perturbation kernel is determined, the score model $\mathbf{s}_{\theta}(\mathbf{x}(t), t)$ can be trained by a network. Unlike VE- and VP-SDEs, the network no longer estimates Gaussian noise of the whole image but only predicts the high-frequency part of Gaussian noise (details in Appendix B):

$$\theta^* = \arg \min_{\theta} \mathbb{E}_t \left\{ \lambda(t) \mathbb{E}_{\mathbf{x}(0)} \mathbb{E}_{\mathbf{x}(t)|\mathbf{x}(0)} \left[\left\| \mathcal{F}_h(\mathbf{z}) + \sqrt{1 - e^{-\frac{1}{2}t^2(\bar{\beta}_{\max}-\bar{\beta}_{\min})-t\bar{\beta}_{\min}}} \mathcal{F}_h(\mathbf{s}_{\theta}(\mathbf{x}(t), t)) \right\|_2^2 \right] \right\} \quad (19)$$

$\lambda(t)$ is the positive weighting function and \mathbf{z} is Gaussian noise. Empirically, our network only predicts high-frequency noise, releasing the ability of the network.

3) Reverse HFS-SDE for MR Reconstruction: Based on Eq. (14), the conditional reverse-time HFS-SDE can be de-

duced as [39]:

$$d\mathbf{x} = \left(-\frac{1}{2}\beta(t)\mathcal{F}_h(\mathbf{x}) - \beta(t)\mathcal{F}_h(\nabla_{\mathbf{x}}\log p_t(\mathbf{x}|\mathbf{y})) \right) dt + \sqrt{\beta(t)}\mathcal{F}_h d\bar{\mathbf{w}} \quad (20)$$

According to Bayes' theorem and Eq. (1), $\nabla_{\mathbf{x}}\log p_t(\mathbf{x}(t)|\mathbf{y})$ can be written as:

$$\begin{aligned} \nabla_{\mathbf{x}}\log p_t(\mathbf{x}(t)|\mathbf{y}) &= \nabla_{\mathbf{x}}\log p_t(\mathbf{x}(t)) + \nabla_{\mathbf{x}}\log p_t(\mathbf{y}|\mathbf{x}(t)) \\ &\approx \mathbf{s}_{\theta^*}(\mathbf{x}(t), t) + \nabla_{\mathbf{x}}\log p_t(\mathbf{y}|\mathbf{x}(t)) \\ &= \mathbf{s}_{\theta^*}(\mathbf{x}(t), t) + \frac{\mathbf{A}^H(\mathbf{y} - \mathbf{A}\mathbf{x}(t))}{\sigma_{\epsilon}^2} \end{aligned} \quad (21)$$

HFS-SDE generates samples through the Predictor-Corrector method (PC Sampling) in [28] (as shown in Alg. 1).

It is important to note that noises are injected into the high-frequency space of the image during the forward HFS-SDE. Therefore, when $t = 1$, the initial value $\mathbf{x}_T \sim \mathcal{N}(\mathbf{F}^{-1}(\mathbf{M}_l\mathbf{y}), \mathcal{F}_h)$ in reverse-time HFS-SDE. With \mathbf{x}_T utilizing the low-frequency data $\mathbf{M}_l\mathbf{y}$, the reverse-time HFS-SDE converges to the actual solution with fewer iterations, thus reducing the time required for the reverse process.

IV. EXPERIMENTS

Algorithm 1 PC Sampling (HFS-SDE).

Require: $\{\beta_i\}_{i=1}^N, \{\alpha_i\}_{i=1}^N, \text{csm}, \hat{\mathbf{y}}, \lambda_1, \lambda_2, r, N, M, \mathbf{M}_u$. \triangleright
 $\text{csm} = \{\text{csm}_1, \dots, \text{csm}_n\}$, M_u is the under-sampling mask

- 1: $\mathbf{x}_N \sim \mathcal{N}(\mathbf{F}^{-1}(\mathbf{M}_I \mathbf{y}), \mathcal{F}_h)$
- 2: **for** $i = N - 1$ to 0 **do**
- 3: $\mathbf{z} \sim \mathcal{N}(\mathbf{0}, \mathbf{I})$
- 4: $\mathbf{g} \leftarrow \mathcal{F}_h(\mathbf{s}_{\theta^*}(\mathbf{x}_{i+1}, i + 1))$
- 5: $\mathbf{G} = \sum_{j=1}^n \text{csm}_j^* \cdot \mathbf{F}^{-1}(\mathbf{F}(\text{csm} \cdot \mathbf{x}_i) \cdot \mathbf{M}_u - \hat{\mathbf{y}})$
- 6: $\epsilon \leftarrow \lambda_1 (\|\mathbf{g}\|_2 / \|\mathbf{G}\|_2)$
- 7: $\mathbf{x}_i \leftarrow \mathbf{x}_{i+1} + \frac{1}{2} \beta_{i+1} \mathcal{F}_h(\mathbf{x}_i) + \beta_{i+1} (\mathbf{g} - \epsilon \mathbf{G}) + \sqrt{\beta_{i+1}} \mathcal{F}_h(\mathbf{z})$
- 8: **for** $k \leftarrow 1$ to M **do**
- 9: $\mathbf{z} \sim \mathcal{N}(\mathbf{0}, \mathbf{I})$
- 10: $\mathbf{g} \leftarrow \mathcal{F}_h(\mathbf{s}_{\theta^*}(\mathbf{x}_i^{k-1}, i))$
- 11: $\mathbf{G} = \sum_{j=1}^n \text{csm}_j^* \cdot \mathbf{F}^{-1}(\mathbf{F}(\text{csm} \cdot \mathbf{x}_i^k) \cdot \mathbf{M}_u - \hat{\mathbf{y}})$
- 12: $\epsilon_1 \leftarrow 2\alpha_i (r \|\mathbf{z}\|_2 / \|\mathbf{g}\|_2)^2$
- 13: $\epsilon_2 \leftarrow \lambda_2 (\|\mathbf{g}\|_2 / \|\mathbf{G}\|_2)$
- 14: $\mathbf{x}_i^k \leftarrow \mathbf{x}_i^{k-1} + \epsilon_1 (\mathbf{g} - \epsilon_2 \mathbf{G}) + \sqrt{2\epsilon_1} \mathcal{F}_h(\mathbf{z})$
- 15: **end for**
- 16: $\mathbf{x}_{i-1}^0 \leftarrow \mathbf{x}_i^M$
- 17: **end for**

return \mathbf{x}_0^0

A. Experimental setup

1) *Experimental Data*: We conducted experiments on the public fastMRI dataset¹ [40], [41]. For the training dataset, we randomly selected 34 individuals from the fastMRI multi-coil knee dataset, and dropped the first six slices from each individual due to poor image quality. A total of 1002 T1-weighted images were finally obtained as the training dataset. We selected two datasets for testing. One was the knee data from 3 individuals selected randomly from the validation dataset and the other one was the brain data from 1 individual. The first six slices of each individual in test data were also discarded. We finally got 95 T1-weighted knee images and 10 T2-weighted brain images. We cropped the image size to 320×320 , and normalized the data by its own standard deviation before inputting it into the score network.

2) *Parameter Configuration*: We compared HFS-SDE with SENSE [4], supervised deep learning method (ISTA-Net) [20], and score-based model (VE-SDE and VP-SDE) [28], with the results of each method tuned to the best. VP-SDE can be regarded as the ablation method of HFS-SDE. In the training stage, ISTA-Net, VE-, VP- and HFS-SDEs were trained with 500 epochs and the noise scale $N = 1000$ for these SDE-based methods. The exponential moving average (EMA) rate was 0.9999 for VP-SDE and HFS-SDE, and 0.999 for VE-SDE. VP-SDE and HFS-SDE controlled the noise level during forward diffusion by setting $\beta_{\max} = 20$, and $\beta_{\min} = 0.1$ in Alg. 1, while VE-SDE controlled the noise level in forward diffusion by setting $\sigma_{\max} = 348$ and $\sigma_{\min} = 0.1$ [42].

The network used in VE-, VP- and HFS-SDEs was the U-

TABLE I: In-Distribution experiments. The average quantitative metrics on the fastMRI knee dataset under 10-fold and 12-fold uniform undersampling.

AF	Methods	NMSE(*e-2)	PSNR (dB)	SSIM(*e-2)
10-fold	SENSE	5.04 ± 4.73	25.28 ± 3.09	52.97 ± 13.94
	ISTA-Net	1.09 ± 0.60	31.28 ± 2.01	85.44 ± 3.15
	VE-SDE	0.91 ± 0.77	32.31 ± 2.10	81.01 ± 7.78
	VP-SDE	0.75 ± 0.38	32.77 ± 1.88	82.85 ± 5.19
	HFS-SDE	0.74 ± 0.40	32.82 ± 1.84	82.46 ± 5.77
12-fold	SENSE	5.43 ± 4.59	24.81 ± 2.82	52.00 ± 12.88
	ISTA-Net	1.63 ± 0.95	29.53 ± 1.85	82.38 ± 3.24
	VE-SDE	1.36 ± 0.88	30.38 ± 1.78	75.50 ± 7.61
	VP-SDE	5.09 ± 6.53	26.76 ± 4.00	76.21 ± 4.18
	HFS-SDE	1.07 ± 0.44	31.12 ± 1.62	79.41 ± 4.72

net architecture improved by Song (i.e. ddpm² in the code of score-based SDEs). In the test stage, all three SDEs used PC sampling to generate samples, where VP- and HFS-SDEs used the Euler-Maruyama method as the Predictor and VE-SDE used the reverse diffusion SDE solver as the Predictor. All three SDEs used annealed Langevin dynamics method as the Corrector.

3) *Performance Evaluation*: Three quantitative metrics, including normalized mean square error (NMSE), the peak signal-to-noise ratio (PSNR), and structural similarity (SSIM) index [43], were used to measure the reconstruction performance. The smaller NMSE, the larger PSNR and SSIM, indicate a better reconstruction.

B. Experimental Results

This subsection shows the reconstruction results of the above methods in the In-Distribution and Out-of-Distribution cases. In addition, we show the performance of HFS-SDE with reduced number of reverse samples iterations.

1) *In-Distribution Experiments*: In the In-Distribution experiments, the anatomy of the training and testing datasets are the same. Score-based SDEs are unsupervised learning methods that only the fully sampled images are used for network training without the paired undersampled data. Therefore, no undersampling pattern is needed for network training in VE-, VP- and HFS-SDEs. For ISTA-Net, the undersampled masks of training and testing are the same.

The reconstruction results of 10-fold uniform undersampling (containing 24 k-space center lines, net acceleration factor = 6) are shown in Fig. 2. The first row shows the reconstruction results of SENSE, ISTA-Net, VE-SDE, VP-SDE, and HFS-SDE, with NMSE, PSNR (dB), and SSIM shown at the bottom of each image. The second row shows the enlarged view of the region of interest (ROI) (indicated by the yellow box in the first row). The SENSE reconstruction is noisy and shows aliasing artifacts. The reconstructed image of ISTA-Net also has aliasing artifacts and is blurred, losing tiny structures. The score-based SDEs methods are significantly better than SENSE and ISTA-Net. Among these three SDE methods, the reconstruction result of VE-SDE generates superfluous details (indicated by the red arrow). Some tiny

¹<https://fastmri.org/>

²https://github.com/yang-song/score_sde_pytorch

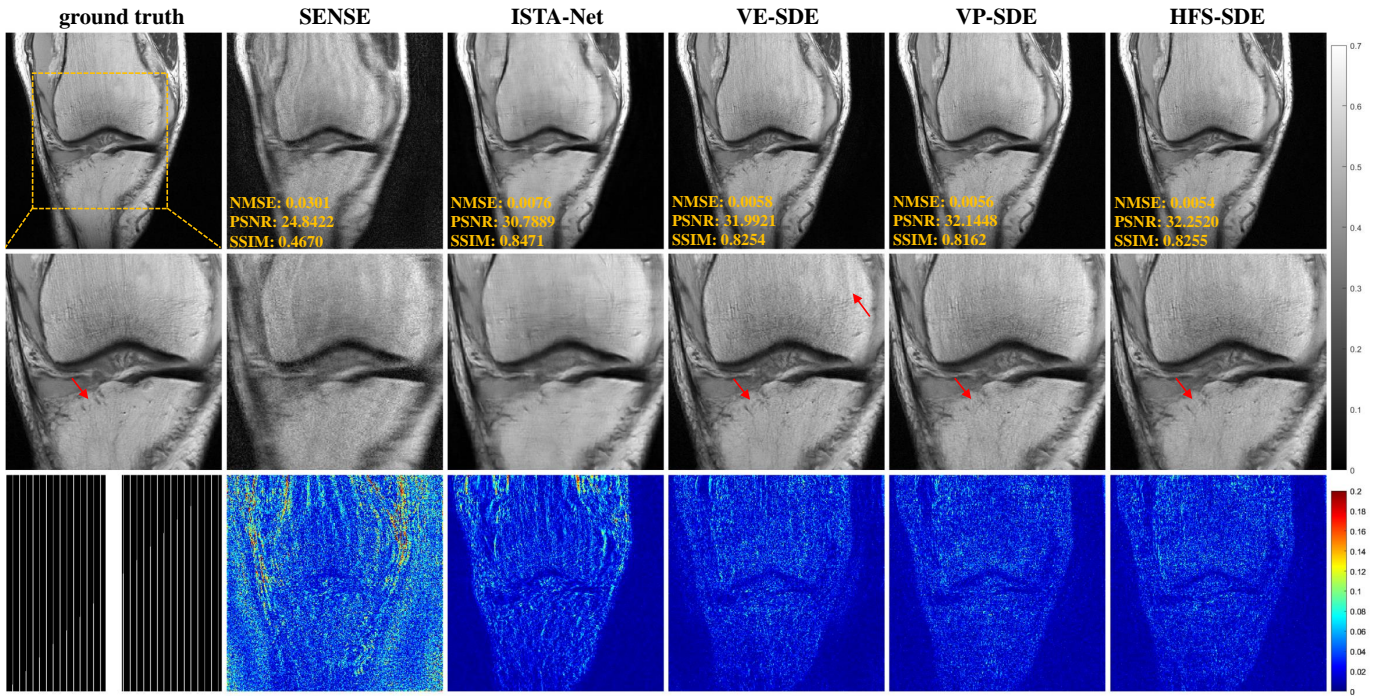


Fig. 2: The reconstruction results of fastMRI multi-coil knee data at uniform undersampling of 10-fold. The first row shows the ground truth and the reconstruction of SENSE, ISTA-Net, VE-SDE, VP-SDE and HFS-SDE (ours). The values at the bottom of the first row indicate NMSE, PSNR (dB) and SSIM. The second row shows the enlarged view of the ROI region (indicated by the yellow box in the first row), and the third row shows the error map of the reconstruction. The undersampling mask used for the test is shown in the lower left corner.

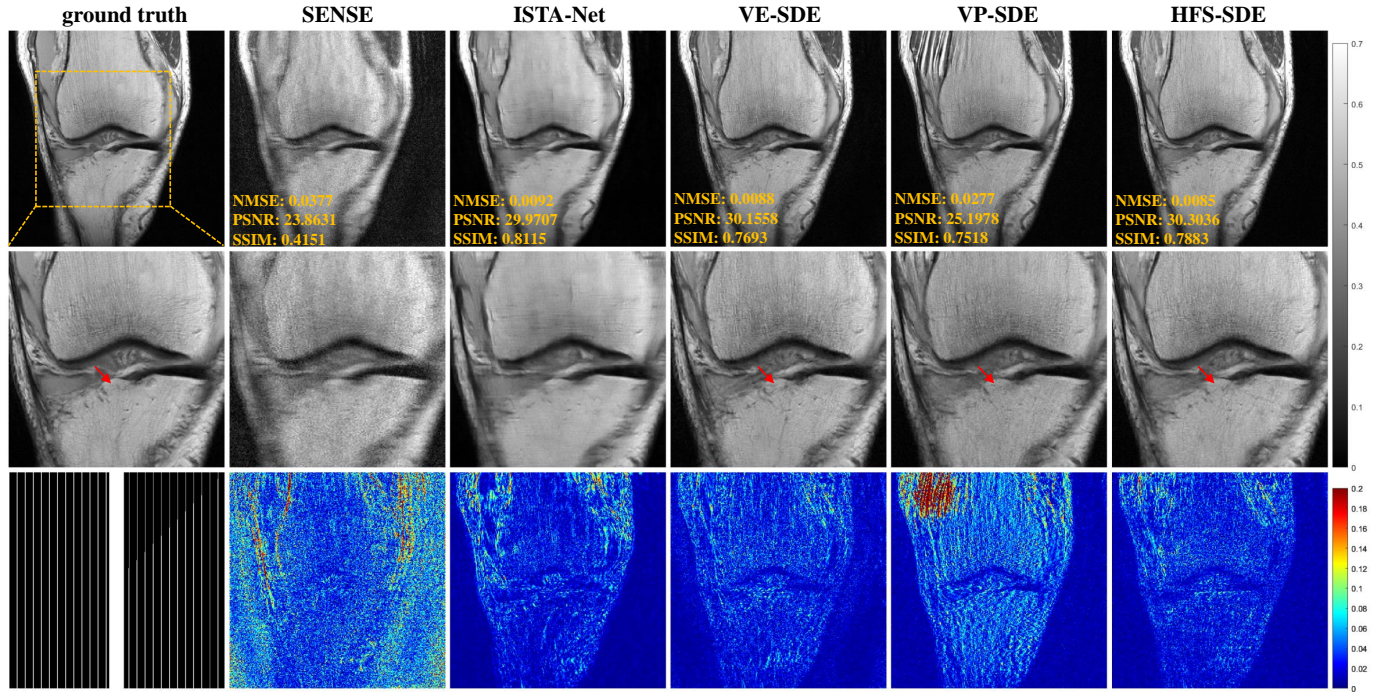


Fig. 3: The reconstruction results of fastMRI multi-coil knee data at uniform undersampling of 12-fold. The first row shows the ground truth and the reconstruction of SENSE, ISTA-Net, VE-SDE, VP-SDE and HFS-SDE (ours). The values at the bottom of the first row indicate NMSE, PSNR (dB) and SSIM. The second row shows the enlarged view of the ROI region (indicated by the yellow box in the first row), and the third row shows the error map of the reconstruction. The undersampling mask used for the test is shown in the lower left corner.

TABLE II: Out-of-Distribution experiments. The average quantitative metrics on the fastMRI brain dataset under 10-fold uniform undersampling.

AF	Methods	NMSE(*e-2)	PSNR (dB)	SSIM(*e-2)
10-fold	SENSE	8.17 \pm 3.96	22.92 \pm 2.36	45.80 \pm 10.62
	ISTA-Net	2.04 \pm 1.04	28.83 \pm 1.43	84.09 \pm 2.22
	VE-SDE	1.27 \pm 0.40	30.63 \pm 1.68	78.00 \pm 7.06
	VP-SDE	1.27 \pm 0.49	30.68 \pm 1.92	82.00 \pm 4.50
	HFS-SDE	1.19 \pm 0.13	30.76 \pm 1.13	79.78 \pm 5.04

TABLE III: Accelerated sampling experiments. The average quantitative metrics on the fastMRI knee dataset under 10-fold uniform random undersampling.

AF	Methods	NMSE(*e-2)	PSNR (dB)	SSIM(*e-2)
10-fold	VE-SDE	2.15 \pm 1.02	28.15 \pm 1.89	75.00 \pm 4.00
	VP-SDE	13.51 \pm 9.55	21.11 \pm 3.42	59.38 \pm 5.05
	HFS-SDE	1.10 \pm 0.37	30.91 \pm 1.66	77.55 \pm 4.39

structures lost in the images reconstructed by VP-SDE. HFS-SDE achieves the best performance in terms of the quantitative metrics, preserving the most realistic high-frequency details and completely suppressing the artifacts.

Fig. 3 shows the reconstruction results using 12-fold uniform undersampling (containing 22 k-space center lines, net acceleration factor = 7). The images reconstructed by SENSE and ISTA-Net show severe blurring and aliasing artifacts. The image reconstructed by VE-SDE degrades fast, which may due to the divergence of SDE sequence at a high acceleration. The result of HFS-SDE shows less reconstruction errors than those using VP- and VE-SDEs. The average quantitative metrics of the knee dataset is shown in Table I. HSF-SDE has the best NMSE and PSNR among all compared methods.

2) Out-of-Distribution Experiments: We conducted experiments on T2-weighted brain data with ISTA-Net and VE-, VP- and HFS-SDEs, using the models trained on T1-weighted knee data. In this scenario, the distribution of testing data is inconsistent with that in training data. The reconstruction results of 10-fold uniform undersampling are shown in Fig. 4. The reconstruction quality of ISTA-Net suffers a serious degradation, while the SDE-based methods maintain high reconstruction quality. HFS-SDE still achieves the best reconstruction result with the least noise and artifacts. Table II shows the quantitative metrics of the test brain dataset.

3) Accelerated Sampling: In the above experiments, the noise scale N of VE-, VP- and HFS-SDEs was 1000. It means 1000 iterations were needed in the reverse-time process for sample generation, taking an average of 2.5 minutes to reconstruct a 320×320 MR image on an NVIDIA RTX A6000 GPU.

To show the ability of accelerating sampling using HSF-SDE, we tested the 10-fold reconstruction of VE-, VP-, and HSF-SDEs by 10× sampling acceleration ($N = 100$). The results are shown in Fig. 5. When the number of reverse sampling iterations is reduced to 100, VE-SDE generates many fake tiny structures and the reconstructed image of VP-SDE shows severe aliasing artifacts. The result of HFS-SDE with $N = 100$ is comparable with that with $N = 1000$ visually, although the quantitative metrics are a bit lower than those

with $N = 1000$. The average quantitative metrics of the knee dataset are shown in Table III. HFS-SDE outperforms VE- and VP-SDEs using the 10× sampling acceleration.

V. DISCUSSION

In this study, the HFS-SDE was proposed for solving the inverse problem in accelerated MRI based on diffusion model. We have demonstrated that diffusion in the high-frequency space effectively improves the stability of VP-SDE. Meanwhile, HSF-SDE reduces the time required for reverse sampling and maintains the reconstruction quality, by utilizing the low-frequency information of MR images.

A. The optimization model of HSF-SDE

The iterative rule of the reverse-time HFS-SDE is

$$\mathbf{x}_i = \mathbf{x}_{i+1} + \frac{1}{2}\beta_{i+1}\mathcal{F}_h(\mathbf{x}_{i+1}) + \beta_{i+1}\mathcal{F}_h(s_{\theta^*}(\mathbf{x}_{i+1}, i+1)) + \sqrt{\beta_{i+1}}\mathcal{F}_h(\mathbf{z}_i), \quad i = 0, 1, \dots, N-1 \quad (22)$$

From an optimization perspective, the reverse-time HFS-SDE can also be treated as a solution to the following optimization problem using the inexact Stochastic gradient Langvien descent algorithm:

$$\max_{\mathbf{x}} \lambda_1 e^{\|\mathcal{F}_h(\mathbf{x})\|^2} + \lambda_2 e^{\log p(\mathbf{x})}, \quad (23)$$

where λ_1 and λ_2 are positive weights. The first term changes from $\lambda_1 e^{\|\mathbf{x}\|^2}$ to $\lambda_1 e^{\|\mathcal{F}_h(\mathbf{x})\|^2}$ compared with the optimization function of VP-SDE in Eq. (10). Since the image energy is mainly concentrated in low-frequency area, the energy in high-frequency space ($\|\mathcal{F}_h(\mathbf{x})\|^2$) is much lower than that in the whole image ($\|\mathbf{x}\|^2$). Eq. (23) would be dominated by the second term, avoiding the energy explosion of \mathbf{x} . Therefore, the possibility of divergence in the iterative sequence is reduced when using HFS-SDE compared with using VP-SDE. Our experiments in this study have demonstrated that HFS-SDE can achieve good performance at a high acceleration rate of 12-fold, while severe artifacts appeared in the reconstructed image using VP-SDE due to the sequence divergence in the diffusion process.

B. Extensions of HSF-SDE

The idea of diffusion in high-frequency space can be extended to other SDEs, such as VE- and sub-VP-SDEs. The corresponding forward SDEs are:

$$\begin{cases} d\mathbf{x} = \sqrt{\frac{d[\sigma^2(t)]}{dt}}\mathcal{F}_h d\mathbf{w} \\ d\mathbf{x} = -\frac{1}{2}\beta(t)\mathcal{F}_h(\mathbf{x})dt + \sqrt{\beta(t)\left(1 - e^{-2\int_0^t \beta(s)ds}\right)}\mathcal{F}_h d\mathbf{w} \end{cases} \quad (24)$$

Then MR reconstructions using these two SDEs will start from the low-resolution image generated from the k-space centre instead of pure Gaussian noise, hence reducing sampling iterations in the reverse process. One major drawback of fast MRI is the loss of details. Diffusion in HFS may help recover high-frequency details on MR images as well.

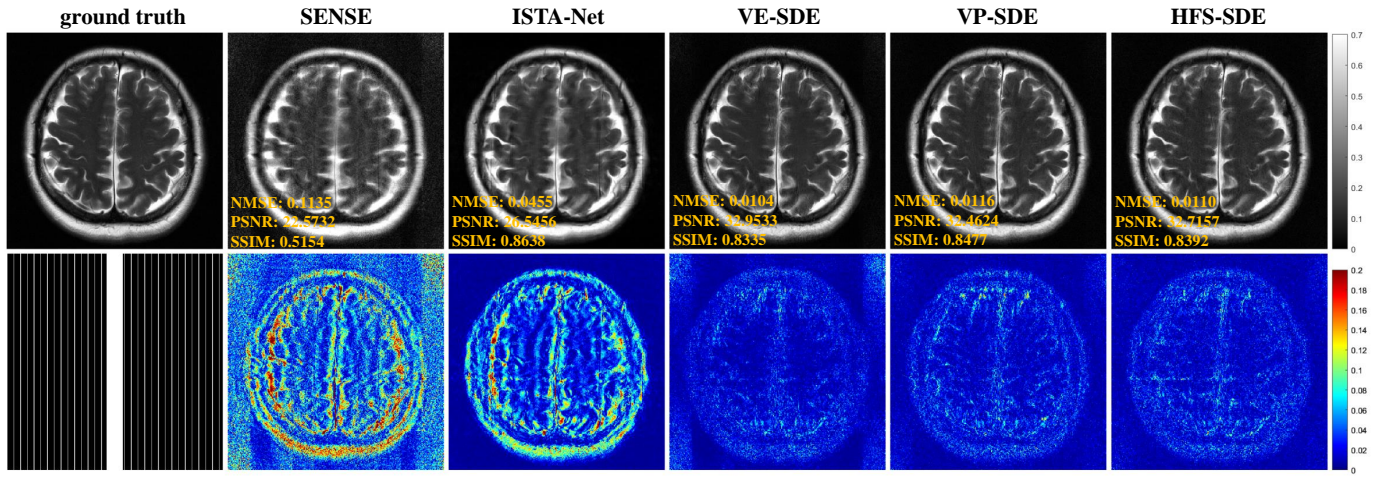


Fig. 4: Out-of-Distribution results. The reconstruction results in the multi-coil, 10-fold under-sampling scene. The first row shows the reconstruction results of SENSE, ISTA-Net, VE-SDE, VP-SDE and HFS-SDE. The yellow numbers at the bottom of the first row indicate PSNR (dB) and SSIM. The second row shows the error map of the ROI region. The under-sampling mask is shown in the lower left corner.

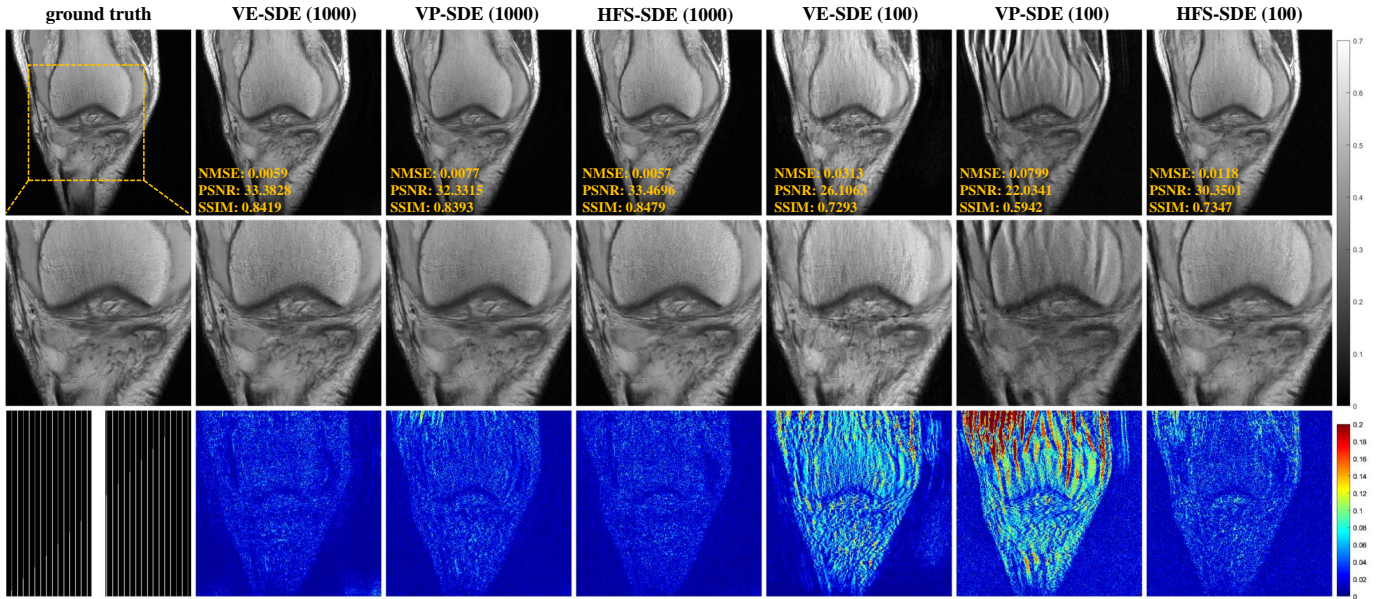


Fig. 5: Accelerated Sampling. The reconstruction results of fastMRI multi-coil knee data at uniform undersampling of 10-fold with only 100 iterations. The first row shows the ground truth and the reconstruction of VE-SDE, VP-SDE and HFS-SDE (ours), where the three rightmost columns are the results of 100 iterations of reconstruction. The values at the bottom of the first row indicate NMSE, PSNR (dB) and SSIM. The second row shows the enlarged view of the ROI region (indicated by the yellow box in the first row), and the third row shows the error map of the reconstruction. The undersampling mask used for the test is shown in the lower left corner.

C. Limitations

There exist several U-Net architectures to estimate the score function in diffusion model, with different skip connections, residual blocks, etc. The choice of the U-Net architecture affects the performance of the diffusion model. In this study, we just used the ddpm provided by song [28] and did not test other network architectures, since our study aims to demonstrate the advantage of diffusion in high-frequency space. For a fair comparison, all three SDE-based reconstruction methods used

the same network architecture in the experiments. A more complicated network may further improve the performance of the proposed method. The test dataset is small in this study. Although we have shown the advantages of HSF-SDE on this test dataset, testing the performance of HSF-SDE on a larger dataset is still needed and will be investigated in our future work.

VI. CONCLUSIONS

A new SDE was proposed for fast MR reconstruction that restricts the diffusion process in high-frequency space. It improves the stability of the diffusion-based MR reconstruction and accelerates the sampling. Our experiments have demonstrated that HFS-SDE based reconstruction method outperforms the parallel imaging, supervised deep learning, existing VE- and VP-SDEs-based methods in terms of reconstruction accuracy.

ACKNOWLEDGEMENT

This study was supported in part by the National Key R&D Program of China nos. 2020YFA0712200, 2021YFF0501402, National Natural Science Foundation of China under grant nos. 81971611, 62125111, U1805261, 62106252, 12026603, the Guangdong Basic and Applied Basic Research Foundation no. 2021A1515110540, Shenzhen Science and Technology Program under grant no. RCYX20210609104444089.

APPENDIX

A. The Forward Diffusion Process of HFS-SDE

This section presents detailed derivation of the forward diffusion process for HFS-SDE. Assuming that there are N noise scales in the forward diffusion process, the following discrete Markov chain constructs the forward diffusion process,:

$$\mathbf{x}_i = \mathcal{F}_l(\mathbf{x}_{i-1}) + \sqrt{1 - \beta_i} \mathcal{F}_h(\mathbf{x}_{i-1}) + \sqrt{\beta_i} \mathcal{F}_h(\mathbf{z}_{i-1}), \quad i = 1, \dots, N \quad (25)$$

$\{\beta_1, \beta_2, \dots, \beta_N\}$ are given coefficients to control the noise level and $\mathbf{z}_{i-1} \sim \mathcal{N}(\mathbf{0}, \mathbf{I})$. By introducing auxiliary variables $\tilde{\beta}_i = N\beta_i$, Eq. (25) can be rewritten as

$$\mathbf{x}_i = \mathcal{F}_l(\mathbf{x}_{i-1}) + \sqrt{1 - \frac{\tilde{\beta}_i}{N}} \mathcal{F}_h(\mathbf{x}_{i-1}) + \sqrt{\frac{\tilde{\beta}_i}{N}} \mathcal{F}_h(\mathbf{z}_{i-1}), \quad i = 1, \dots, N \quad (26)$$

When $N \rightarrow \infty$ and $t \in [0, 1]$, $\{\tilde{\beta}_i\}_{i=1}^N$ can be written as $\{\beta(t)\}_{t=0}^1$, $\{\mathbf{z}_{i=1}^N\}$ become $\{\mathbf{z}(t)\}_{t=0}^1$ and $\{\mathbf{x}_{i=1}^N\}$ become a continuous process $\{\mathbf{x}(t)\}_{t=0}^1$. Let $\Delta t = \frac{1}{N} \rightarrow 0$,

$$\begin{aligned} \mathbf{x}(t + \Delta t) &= \mathcal{F}_l(\mathbf{x}(t)) + \sqrt{1 - \beta(t + \Delta t)\Delta t} \mathcal{F}_h(\mathbf{x}(t)) \\ &\quad + \sqrt{\beta(t + \Delta t)\Delta t} \mathcal{F}_h(\mathbf{z}(t)) \\ &\approx \mathcal{F}_l(\mathbf{x}(t)) + \mathcal{F}_h(\mathbf{x}(t)) - \frac{1}{2}\beta(t + \Delta t)\Delta t \mathcal{F}_h(\mathbf{x}(t)) \\ &\quad + \sqrt{\beta(t + \Delta t)\Delta t} \mathcal{F}_h(\mathbf{z}(t)) \\ &\approx \mathbf{x}(t) - \frac{1}{2}\beta(t)\Delta t \mathcal{F}_h(\mathbf{x}(t)) + \sqrt{\beta(t)\Delta t} \mathcal{F}_h(\mathbf{z}(t)) \end{aligned} \quad (27)$$

Eq. (27) converges to

$$d\mathbf{x} = -\frac{1}{2}\beta(t)\mathcal{F}_h(\mathbf{x})dt + \sqrt{\beta(t)}\mathcal{F}_h d\mathbf{w} \quad (28)$$

B. Estimate Score for HFS-SDE

The score model $\mathbf{s}_\theta(\mathbf{x}(t), t)$ can be trained via score matching to estimate score function $\log p_{0t}(\mathbf{x}(t) | \mathbf{x}(0))$:

$$\theta^* = \arg \min_{\theta} \mathbb{E}_t \left\{ \lambda(t) \mathbb{E}_{\mathbf{x}(0)} \mathbb{E}_{\mathbf{x}(t)|\mathbf{x}(0)} \left[\left\| \mathbf{s}_\theta(\mathbf{x}(t), t) - \nabla_{\mathbf{x}(t)} \log p_{0t}(\mathbf{x}(t) | \mathbf{x}(0)) \right\|_2^2 \right] \right\} \quad (29)$$

$\lambda(t)$ is the positive weighting function. By Eq. (18), Eq. (29) can be rewritten as:

$$\theta^* = \arg \min_{\theta} \mathbb{E}_t \left\{ \lambda(t) \mathbb{E}_{\mathbf{x}(0)} \mathbb{E}_{\mathbf{x}(t)|\mathbf{x}(0)} \left[\left\| \mathbf{z} + \sqrt{\left(1 - e^{-\frac{1}{2}t^2(\tilde{\beta}_{\max} - \tilde{\beta}_{\min}) - t\tilde{\beta}_{\min}}\right)} \mathcal{F}_h(\mathbf{s}_\theta(\mathbf{x}(t), t)) \right\|_2^2 \right] \right\} \quad (30)$$

$\mathbf{z} \sim \mathcal{N}(\mathbf{0}, \mathbf{I})$. Since $\mathcal{F}_h(\cdot)^{\frac{1}{2}} = \mathcal{F}_h(\cdot)$, we finally trained the network with following loss:

$$\theta^* = \arg \min_{\theta} \mathbb{E}_t \left\{ \lambda(t) \mathbb{E}_{\mathbf{x}(0)} \mathbb{E}_{\mathbf{x}(t)|\mathbf{x}(0)} \left[\left\| \mathcal{F}_h(\mathbf{z}) + \sqrt{\left(1 - e^{-\frac{1}{2}t^2(\tilde{\beta}_{\max} - \tilde{\beta}_{\min}) - t\tilde{\beta}_{\min}}\right)} \mathcal{F}_h(\mathbf{s}_\theta(\mathbf{x}(t), t)) \right\|_2^2 \right] \right\} \quad (31)$$

REFERENCES

- [1] J. P. Haldar, D. Hernando, and Z.-P. Liang, "Compressed-sensing mri with random encoding," *IEEE Transactions on Medical Imaging*, vol. 30, no. 4, pp. 893–903, 2010.
- [2] K. H. Jin, D. Lee, and J. C. Ye, "A general framework for compressed sensing and parallel mri using annihilating filter based low-rank hankel matrix," *IEEE Transactions on Computational Imaging*, vol. 2, no. 4, pp. 480–495, 2016.
- [3] A. Majumdar, "Improving synthesis and analysis prior blind compressed sensing with low-rank constraints for dynamic mri reconstruction," *Magnetic Resonance Imaging*, vol. 33, no. 1, pp. 174–179, 2015.
- [4] K. P. Pruessmann, M. Weiger, M. B. Scheidegger, and P. Boesiger, "Sense: sensitivity encoding for fast mri," *Magnetic Resonance in Medicine*, vol. 42, no. 5, pp. 952–962, 1999.
- [5] M. A. Griswold, P. M. Jakob, R. M. Heidemann, M. Nittka, V. Jellus, J. Wang, B. Kiefer, and A. Haase, "Generalized autocalibrating partially parallel acquisitions (grappa)," *Magnetic Resonance in Medicine*, vol. 47, no. 6, pp. 1202–1210, 2002.
- [6] M. Lustig and J. M. Pauly, "Spirit: iterative self-consistent parallel imaging reconstruction from arbitrary k-space," *Magnetic Resonance in Medicine*, vol. 64, no. 2, pp. 457–471, 2010.
- [7] S. G. Lingala, Y. Hu, E. DiBella, and M. Jacob, "Accelerated dynamic mri exploiting sparsity and low-rank structure: k-t slr," *IEEE Transactions on Medical Imaging*, vol. 30, no. 5, pp. 1042–1054, 2011.
- [8] C. Y. Lin and J. A. Fessler, "Efficient dynamic parallel mri reconstruction for the low-rank plus sparse model," *IEEE Transactions on Computational Imaging*, vol. 5, no. 1, pp. 17–26, 2019.
- [9] B. Zhao, J. P. Haldar, A. G. Christodoulou, and Z.-P. Liang, "Image reconstruction from highly undersampled (k, t)-space data with joint partial separability and sparsity constraints," *IEEE Transactions on Medical Imaging*, vol. 31, no. 9, pp. 1809–1820, 2012.
- [10] P. Huang, C. Zhang, X. Zhang, X. Li, L. Dong, and L. Ying, "Unsupervised deep unrolled reconstruction using regularization by denoising," *arXiv preprint arXiv:2205.03519*, 2022.
- [11] S. Wang, Z. Su, L. Ying, X. Peng, S. Zhu, F. Liang, D. Feng, and D. Liang, "Accelerating magnetic resonance imaging via deep learning," in *2016 IEEE 13th International Symposium on Biomedical Imaging*. IEEE, 2016, pp. 514–517.
- [12] D. Liang, J. Cheng, Z. Ke, and L. Ying, "Deep magnetic resonance image reconstruction: Inverse problems meet neural networks," *IEEE Signal Processing Magazine*, vol. 37, no. 1, pp. 141–151, 2020.
- [13] Y. Han, L. Sunwoo, and J. C. Ye, "k-space deep learning for accelerated mri," *IEEE Transactions on Medical Imaging*, vol. 39, no. 2, pp. 377–386, 2019.
- [14] X. Peng, B. P. Sutton, F. Lam, and Z.-P. Liang, "DeepSense: Learning coil sensitivity functions for sense reconstruction using deep learning," *Magnetic Resonance in Medicine*, vol. 87, no. 4, pp. 1894–1902, 2022.

- [15] G. Oh, B. Sim, H. Chung, L. Sunwoo, and J. C. Ye, "Unpaired deep learning for accelerated mri using optimal transport driven cyclegan," *IEEE Transactions on Computational Imaging*, vol. 6, pp. 1285–1296, 2020.
- [16] U. Nakarmi, J. Y. Cheng, E. P. Rios, M. Mardani, J. M. Pauly, L. Ying, and S. S. Vasanawala, "Multi-scale unrolled deep learning framework for accelerated magnetic resonance imaging," in *2020 IEEE 17th International Symposium on Biomedical Imaging (ISBI)*. IEEE, 2020, pp. 1056–1059.
- [17] P. Huang, C. Zhang, H. Li, S. K. Gaire, R. Liu, X. Zhang, X. Li, and L. Ying, "Deep mri reconstruction without ground truth for training," in *Proceedings of 27th Annual Meeting of ISMRM2019*, 2019.
- [18] H. K. Aggarwal, M. P. Mani, and M. Jacob, "Modl: Model-based deep learning architecture for inverse problems," *IEEE Transactions on Medical Imaging*, vol. 38, no. 2, pp. 394–405, 2018.
- [19] J. Sun, H. Li, Z. Xu *et al.*, "Deep admm-net for compressive sensing mri," *Advances in Neural Information Processing Systems*, vol. 29, 2016.
- [20] J. Zhang and B. Ghanem, "Ista-net: Interpretable optimization-inspired deep network for image compressive sensing," in *Proceedings of the IEEE Conference on Computer Vision and Pattern Recognition*, 2018, pp. 1828–1837.
- [21] Z.-X. Cui, J. Cheng, Q. Zhu, Y. Liu, S. Jia, K. Zhao, Z. Ke, W. Huang, H. Wang, Y. Zhu *et al.*, "Equilibrated zeroth-order unrolled deep networks for accelerated mri," *arXiv preprint arXiv:2112.09891*, 2021.
- [22] P. Dhariwal and A. Nichol, "Diffusion models beat gans on image synthesis," *Advances in Neural Information Processing Systems*, vol. 34, pp. 8780–8794, 2021.
- [23] A. Q. Nichol and P. Dhariwal, "Improved denoising diffusion probabilistic models," in *International Conference on Machine Learning*. PMLR, 2021, pp. 8162–8171.
- [24] R. Rombach, A. Blattmann, D. Lorenz, P. Esser, and B. Ommer, "High-resolution image synthesis with latent diffusion models," in *Proceedings of the IEEE/CVF Conference on Computer Vision and Pattern Recognition*, 2022, pp. 10 684–10 695.
- [25] L. Yang, Z. Zhang, Y. Song, S. Hong, R. Xu, Y. Zhao, Y. Shao, W. Zhang, B. Cui, and M.-H. Yang, "Diffusion models: A comprehensive survey of methods and applications," *arXiv preprint arXiv:2209.00796*, 2022.
- [26] J. Ho, A. Jain, and P. Abbeel, "Denoising diffusion probabilistic models," *Advances in Neural Information Processing Systems*, vol. 33, pp. 6840–6851, 2020.
- [27] Y. Song and S. Ermon, "Generative modeling by estimating gradients of the data distribution," *Advances in Neural Information Processing Systems*, vol. 32, 2019.
- [28] Y. Song, J. Sohl-Dickstein, D. P. Kingma, A. Kumar, S. Ermon, and B. Poole, "Score-based generative modeling through stochastic differential equations," in *International Conference on Learning Representations*, 2021. [Online]. Available: <https://openreview.net/forum?id=PxTIG12RRHS>
- [29] A. Jalal, M. Arvinte, G. Daras, E. Price, A. G. Dimakis, and J. Tamir, "Robust compressed sensing mri with deep generative priors," *Advances in Neural Information Processing Systems*, vol. 34, pp. 14 938–14 954, 2021.
- [30] Y. Song, L. Shen, L. Xing, and S. Ermon, "Solving inverse problems in medical imaging with score-based generative models," in *International Conference on Learning Representations*, 2022. [Online]. Available: <https://openreview.net/forum?id=vaRCHVj0uGI>
- [31] H. Chung and J. C. Ye, "Score-based diffusion models for accelerated mri," *Medical Image Analysis*, p. 102479, 2022.
- [32] B. Kim and J. C. Ye, "Diffusion deformable model for 4d temporal medical image generation," in *International Conference on Medical Image Computing and Computer-Assisted Intervention*. Springer, 2022, pp. 539–548.
- [33] Z.-X. Cui, C. Cao, S. Liu, Q. Zhu, J. Cheng, H. Wang, Y. Zhu, and D. Liang, "Self-score: Self-supervised learning on score-based models for mri reconstruction," *arXiv preprint arXiv:2209.00835*, 2022.
- [34] S. U. Dar, Ş. Öztürk, Y. Korkmaz, G. Elmas, M. Özbey, A. Güngör, and T. Çukur, "Adaptive diffusion priors for accelerated mri reconstruction," *arXiv preprint arXiv:2207.05876*, 2022.
- [35] H. Chung, B. Sim, and J. C. Ye, "Come-closer-diffuse-faster: Accelerating conditional diffusion models for inverse problems through stochastic contraction," in *Proceedings of the IEEE/CVF Conference on Computer Vision and Pattern Recognition*, 2022, pp. 12 413–12 422.
- [36] Z. Tu, D. Liu, X. Wang, C. Jiang, M. Zhang, Q. Liu, and D. Liang, "Wkgm: Weight-k-space generative model for parallel imaging reconstruction," *arXiv preprint arXiv:2205.03883*, 2022.
- [37] H. Peng, C. Jiang, Y. Guan, J. Cheng, M. Zhang, D. Liang, and Q. Liu, "One-shot generative prior learned from hankel-k-space for parallel imaging reconstruction," *arXiv preprint arXiv:2208.07181*, 2022.
- [38] S. Särkkä and A. Solin, *Applied Stochastic Differential Equations*. Cambridge University Press, 2019, vol. 10.
- [39] B. D. Anderson, "Reverse-time diffusion equation models," *Stochastic Processes and their Applications*, vol. 12, no. 3, pp. 313–326, 1982.
- [40] J. Zbontar, F. Knoll, A. Sriram, T. Murrell, Z. Huang, M. J. Muckley, A. Defazio, R. Stern, P. Johnson, M. Bruno *et al.*, "fastmri: An open dataset and benchmarks for accelerated mri," *arXiv preprint arXiv:1811.08839*, 2018.
- [41] F. Knoll, J. Zbontar, A. Sriram, M. J. Muckley, M. Bruno, A. Defazio, M. Parente, K. J. Geras, J. Katsnelson, H. Chandarana *et al.*, "fastmri: A publicly available raw k-space and dicom dataset of knee images for accelerated mr image reconstruction using machine learning," *Radiology. Artificial Intelligence*, vol. 2, no. 1, 2020.
- [42] Y. Song and S. Ermon, "Improved techniques for training score-based generative models," *Advances in Neural Information Processing Systems*, vol. 33, pp. 12 438–12 448, 2020.
- [43] Z. Wang, A. C. Bovik, H. R. Sheikh, and E. P. Simoncelli, "Image quality assessment: from error visibility to structural similarity," *IEEE Transactions on Image Processing*, vol. 13, no. 4, pp. 600–612, 2004.